

Characterizations of Magnetic Field Distributions inside Buckling Pipelines

Yu Zhang, Yameng Xue, Xinjing Huang*, Jian Li, and Shili Chen

State Key Laboratory of Precision Measuring Technology and Instruments
Tianjin University, Tianjin 300072, China

zhangyu@tju.edu.cn, xueyameng@tju.edu.cn, *huangxinjing@tju.edu.cn, tjupipe@tju.edu.cn, slchen@tju.edu.cn

Abstract — High internal temperature and pressure often induces the subsea pipelines to buckle and then crack. This paper exposes the magnetic field distribution characterizations inside buckling pipelines in order to detect the buckling via magnetic measurements. J-A force-magnetic coupling model is used to obtain the permeability μ_r as a function of the stress σ . Finite element method with multiphysics coupling is deployed to calculate the magnetic fields inside the buckling pipe with different magnetizations, temperatures, and pressures by importing the μ_r - σ curve. The results demonstrate that complicated stress fields cause the magnetic fields inside the buckling pipe to have many noticeable characteristics that can be deployed to reliably and precisely identify the buckling. The signs and magnitudes of the buckling stress vary significantly in different cross-sections, and even reverse at the buckling starts, where the axial and radial components have two peaks and two peak-valley-peaks symmetrically distributed about the middle plane, respectively. The magnetic fields can reveal tiny buckling with stress but without visible deformation.

Index Terms — Buckling, detection, magnetic field, magnetomechanical effect, subsea pipeline.

I. INTRODUCTION

Subsea pipelines are the most efficient method for continuously transporting offshore crude oil over a long distance. In order to prevent the internal crude oil from condensation, subsea pipelines are usually operated under high temperature and high pressure, having the subsea pipelines suffer great axial and hoop stresses [1]. When the axial stress exceeds the critical value, pipeline buckling occurs, as shown in Fig. 1.

Pipeline buckling deformation is very harmful and dangerous. It can directly lead to pipeline ruptures and leakages via causing the tensile stress over the ultimate yield strength at the outer side of the buckling section. It can also speed up the pipeline aging, as the buckled section suffers serious stress corrosion resulting from the existence of micro-cracks at the stress concentration area. Therefore, it is very significant to periodically, frequently, and timely detect the subsea pipeline buckling.



Fig. 1. Examples of vertical and lateral bucklings of subsea pipelines [1].

Underwater robot with sonar or underwater cameras, such as ROV (Remotely Operated Vehicle) and AUV (Autonomous Underwater Vehicle) [2-4], can be used for pipe buckling detections. Only very large bucklings can be detected, and the cost is very high. The difficulty and cost of deploying ROV and AUV will sharply increase with the increase of depth. Inner PIGs (Pipeline Inspection Gauges) [5-6] with inertial navigation can be used to measure the pipeline trajectory and is capable to identify the buckling sections based on the local abrupt change of the trajectory. However, sophisticated navigation systems and GPS [7-8] are required for PIGs to accurately measure the trajectory alone over a long distance so as to sensitively detect the buckling.

The magnetic fields inside pipelines with various directions have been measured and successfully employed to calculate pipeline orientations and geographical coordinates [9-11]. Since buckling pipelines have distinct geometric shape with non-constant directions, the inside magnetic fields should have some distinctive features. In addition, the stress distributions of the buckling sections are totally different from that of the straight sections. Due to the magnetomechanical effect that magnetization of ferromagnetic materials immersed in ambient magnetic fields can be changed by the stress [12], the magnetization or the equivalent permeability of the pipe wall can be changed by the pipeline buckling deformation. The magnetic fields inside the buckling sections may present special distribution characteristics, and are potential to be utilized for buckling detections.

The objective of this paper is to expose the magnetic field distribution characterizations inside buckling pipelines in order to detect the buckling via magnetic

measurements. First, the J-A force-magnetic coupling model [13], [14] is used to describe the magnetomechanical effect of the pipe steel, and calculate the permeability of the pipe steel under different stress. Second, finite element method is used to model temperature-force-magnetic multiphysics couplings existing in the buckling sections with different orientations, temperatures, and pressures, and calculate the inside magnetic field distributions by importing the calculated permeability. Third, magnetic characterizations of the buckling sections are extracted, discussed, and summarized for pipeline buckling detections, especially for the tiny bucklings, based on the magnetomechanical effect.

II. MAGNETIC PERMEABILITY CALCULATION PRINCIPLE

When an external magnetic field is applied to the ferromagnetic material, the free energy A of the material can be expressed as [13], [14]:

$$A = \mu_0 H M + \frac{\mu_0}{2} \alpha M^2 + \frac{3}{2} \sigma \lambda + T S, \quad (1)$$

where, $\mu_0 = 4\pi \times 10^{-7}$ H/m is the permeability of the air, H is the external magnetic field, M is the magnetization of the material, $\alpha = 0.001$ [15] is the coupling parameter, σ is the stress, λ is the magnetostrictive coefficient, T is the temperature, and S is the entropy. The effective magnetic field is expressed as the derivative of the energy to the external magnetic field [15]:

$$H_e = \frac{1}{\mu_0} \frac{dA}{dM} = H + \alpha M + \frac{3\sigma}{2\mu_0} \frac{d\lambda}{dM}. \quad (2)$$

As the magnetostrictive coefficient is experimentally demonstrated to be the even function of the magnetization M in the J-A force-magnetic coupling model [16], $\gamma = (\gamma_1 + \gamma_1' \sigma) M^2 + (\gamma_2 + \gamma_2' \sigma) M^4$, we can get:

$$H_e = H + \alpha M + \frac{3\sigma}{\mu_0} \left[(\gamma_1 + \gamma_1' \sigma) M + 2(\gamma_2 + \gamma_2' \sigma) M^3 \right], \quad (3)$$

where $\gamma_1 = 7 \times 10^{-18} \text{ A}^{-2} \text{ m}^2$, $\gamma_1' = -1 \times 10^{-25} \text{ A}^{-2} \text{ m}^2 \text{ Pa}^{-1}$, $\gamma_2 = -3.3 \times 10^{-30} \text{ A}^{-4} \text{ m}^4$, and $\gamma_2' = -2.1 \times 10^{-38} \text{ A}^{-4} \text{ m}^4 \text{ Pa}^{-1}$ [15] are the magnetostrictive parameters.

The non-hysteresis magnetizations are equivalent under the two conditions of the external magnetic field with non-zero stress and the equivalent magnetic field with zero stress [15]:

$$M_{an}(H, \sigma) = M_{an}(H_e, 0) = M_s \left[\coth\left(\frac{H_e}{a}\right) - \frac{a}{H_e} \right], \quad (4)$$

where the Langevin function is used for expressing the non-hysteresis magnetization curve; $M_s = 1.7 \times 10^6$ A/m and $a = 1000$ A/m are the planning constant and the saturation magnetization of the material, respectively.

The following relationships exist among the magnetization M , the non-hysteresis magnetization M_{an} , and, the irreversible magnetization M_{irr} [15]:

$$\begin{cases} M = c(M_{an} - M_{irr}) + M_{irr} \\ dM_{irr} = \frac{1}{\xi} \frac{\sigma}{E} (M_{an} - M_{irr}) d\sigma \end{cases}, \quad (5)$$

where $E = 200$ GPa and $\xi = 24.5$ kPa are the Young's modulus and the energy correlation coefficient of the ferromagnetic material, respectively; $c = 0.1$ is the ratio of the initial magnetic susceptibility and the initial non-hysteresis susceptibility.

Then the expression of J-A force-magnetic coupling model can be deduced from (5):

$$\frac{dM}{d\sigma} = \frac{\sigma}{\xi E} (M_{an} - M) + c \frac{dM_{an}}{d\sigma}. \quad (6)$$

The relationship between the magnetization M and the stress σ can be obtained from the force-magnetic coupling model by substituting (2) into (4) and then substituting (4) into (6). According to the definition as shown in (7) [17], the relative permeability μ_r as a function of the stress σ can be numerically calculated, and the result is shown in Fig. 2. This curve will be then imported into the finite element simulation model in the form of look-up table with a stress step of 0.1 MPa:

$$\mu_r = \frac{M}{H} + 1. \quad (7)$$

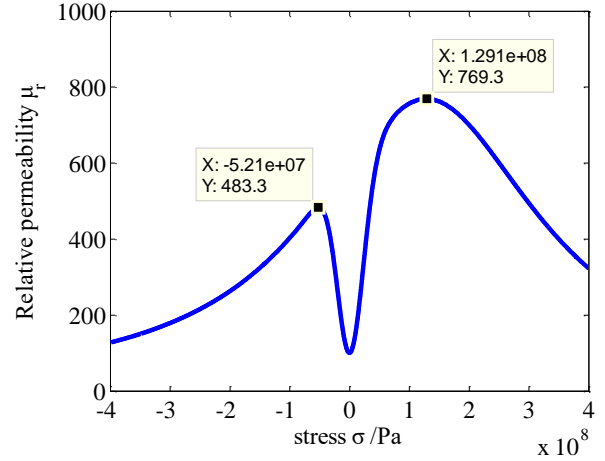


Fig. 2. Relative permeability vs. stress.

III. FINITE ELEMENT MODELING

This paper uses COMSOL software for simulation analyses as follows:

1) Establish the geometrical model, which consists of an air domain and a scaled down buckling pipe, the steel domain, as shown in Fig. 3. The length, width and height of the air domain are all 3m. The buckling pipe consists of two 700mm straight sections and a 1400mm long cosine buckling section. The buckling deflection is 200mm.

2) Set material properties. The relative permeability of the air domain is 1. For the steel domain, the thermal

conductivity is $44.5 \text{ Wm}^{-1}\text{K}^{-1}$; the thermal expansion coefficient is $1.23 \times 10^{-5} \text{ K}^{-1}$; the density is 7850 kg/m^3 ; the Young's modulus is 200 GPa ; the Poisson's ratio is 0.3 ; and the relative permeability at each point is obtained from Fig. 2.

3) Add physics field, including pressure load, thermal load, external magnetic field, and constraints, as shown in Fig. 3. Two ends of the pipeline are set as fixed constraints to accumulate thermal stress. Pressures are added onto the inner and outer surfaces to act as oil pressure and water pressure, respectively. When the heat transfer, from the crude oil to the pipe and then to the water, stabilizes, both the temperatures of the internal and external surfaces tend to be stable. Therefore, the temperatures of the pipe surfaces are configured as the stationary values in the simulation. The heat transfer model and the stationary temperatures of heated oil pipelines can be obtained from ref. [18]. The thermal stress is determined by the thermal expansion coefficient. The background magnetic field $H_b = (H_{xb}, H_{yb}, H_{zb})$ can be described as follows:

$$H_{xb} = H_b \cos I \sin D, H_{yb} = H_b \cos I \cos D, H_{zb} = -H_b \sin I, (8)$$

where I is the inclination angle between H_b and the x - y plane, and D is the angle between the component of H_b on the x - y plane and the y axis, as shown in the top right of Fig. 3. H_b is 40 A/m . The outer surfaces of the air domain are set as *External Magnetic Flux Density* boundary condition to force the total field to be equal to the background field on the external boundaries.

4) Carry on meshing, all the domains are meshed

into tetrahedral and triangular elements with an “Extra fine” mesh size configuration. Add steady state study to simulation before solving, then calculating, and post-processing the results.

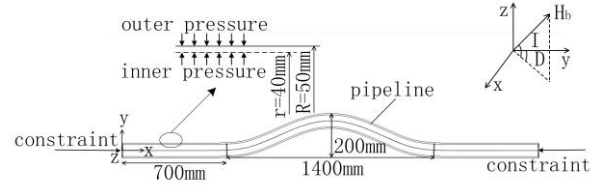


Fig. 3. Simulation model.

IV. RESULTS AND DISCUSSIONS

A. Magnetic field distributions inside the buckling pipe

One scenario with $I = 45^\circ$ and $D = 90^\circ$ is calculated for straight, deformed, and buckling pipes. Parametric sweeping will be carried out later. For the buckling pipe, a typical set of simulation parameters are chosen: the internal pressure is 10 MPa , the external pressure is 0.3 MPa , and the working temperature is 80°C . Calculation results are shown in Fig. 4. The magnetic fields inside the middle section are closer to that inside an actual infinitely long pipeline without magnetic sudden changes near the two ends. Therefore, the simulation results are trimmed off by 250 mm from the two ends with only the middle part preserved and presented in the following discussions.

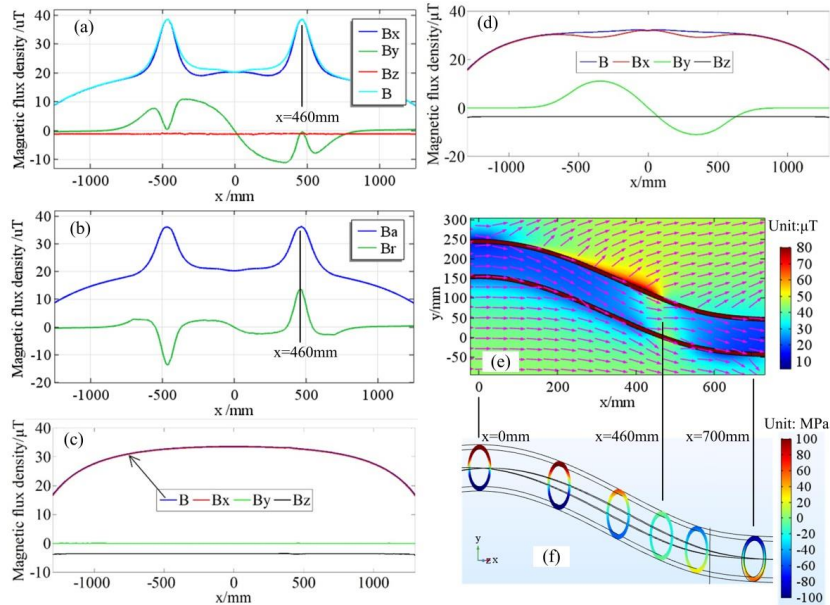


Fig. 4. Simulation results for a typical scenario with $I = 45^\circ$, $D = 90^\circ$, internal pressure of 10 MPa , and temperature of 80°C . Magnetic field distributions inside: (a) buckling, (c) straight, and (d) deformed pipes in the Cartesian coordinate system, and inside the (b) buckling pipe in the cylindrical coordinate system. (e) Intensity and normalized vector plot of the magnetic fields inside the buckling section. (f) Stress fields in different cross-sections.

The magnetic fields inside the three pipes are different. First, they have different distribution shapes. For the buckling pipe, as shown in Fig. 4 (a), B_x has two noticeable peaks at the position $x=\pm 460$ mm and B_y has four peaks and two valleys near the position $x=\pm 460$ mm symmetrically distributed about the $x=0$ plane, and each valley locates between two peaks. In the cylindrical coordinate system, as shown in Fig. 4 (b), the axial and radial magnetic components also have narrow and noticeable peaks. The magnetic fields inside the straight pipe are flat and smooth without any noticeable characteristics in terms of spatial distributions, as shown in Fig. 4 (c). For the deformed but not stressed pipe, as shown in Fig. 4 (d), B_x has two small valleys with one small peak between them, and B_y has two blunt peaks symmetrically distributed about the $x=0$ plane without valleys.

Second, the magnetic fields inside the three pipes have different intensities. The flat part of B curve is smaller than that inside the deformed but not stressed pipe and the straight pipe. In terms of the components, the amplitude of B_z reduces to $1\mu\text{T}$ from the original $4\mu\text{T}$ compared with the straight and deformed pipes. This indicates that when the pipe is buckling and stressed, the magnetic shielding of the pipe is enhanced as the equivalent permeability overall becomes larger due to the magnetomechanical effect.

It is pretty interesting that the B and B_x peaks and B_y valleys occur at $x=\pm 460$ mm, where the bend starts. The magnetic intensity and normalized vector plot, as shown in Fig. 4 (e), demonstrates that the magnetic intensity is larger near the buckling start than that at other areas inside the buckling pipe. The magnetic fields near the buckling start are parallel to the background magnetic fields or x axis, while the magnetic fields at other sections are parallel to the pipe axis. This is due to the complicated and special stress field distributions on different cross-sections, as shown in Fig. 4 (f). The polarity of the stress field is reversed at the bend start ($x=460$ mm), where the stress is almost zero. When $x>460$ mm, the stress is compressional and tensile in the upper and lower sides of the pipe, respectively; while when $x<460$ mm, the stress converts into being tensile and compressional in the upper and lower sides. Therefore, under the action of the magnetomechanical effect, the extreme existence of the stress makes B and B_x reach their maximum values.

Figure 5 shows the magnetic field distributions on different measurement lines with different distances from the pipe axis when the buckling pipe is loaded with high pressure and temperature. These measurement lines are parallel to the pipe axis. Figure 5 (a) shows the magnetic field distributions on different lines of $z>0$ in the x - z plane inside the pipeline, and Fig. 5 (b) shows the magnetic field distributions on different lines in the x - y plane inside the pipeline. Lift-off values have little

effects on the magnetic field distributions, in terms of both the distribution shape and amplitude. Therefore, in the following parts of this paper, we will use the magnetic fields on the central axis to analyze and discuss the magnetic field distribution characteristics inside buckling pipes under different parametric conditions.

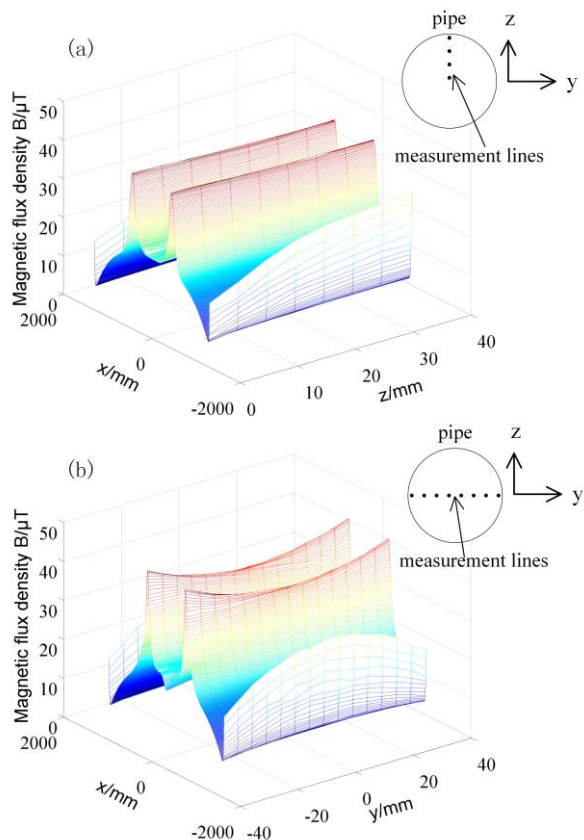


Fig. 5. Magnetic field distributions on different measuring lines parallel to the axis in the x - z (a) and x - y (b) planes.

B. Effects of ambient field direction

Parametric sweepings are performed for I and D with a range of $0\sim 90^\circ$ and a step of 10° in order to expose how ambient field direction affects the magnetic fields inside a buckling pipe. When $I = 0^\circ$ and $D = 0^\circ$, the ambient field is perpendicular to the pipe; when $I = 0^\circ$ and $D = 90^\circ$, the ambient field is parallel to the pipe. Due to there are too many combinations of I and D , here we only present the results of the scenarios with $I = 0^\circ$ and $D = 0\sim 90^\circ$, as shown in Fig. 6. The internal pressure is 10 MPa. The pipe temperature is 80°C .

B_x is much larger than B_y and B_z , so B_x and the norm B have similar distribution shapes, as shown in Figs. 6 (a) and (c), and both of them have two peaks at the two start points of the buckling section. B_y has four peaks and two valleys symmetrically distributed about the $x=0$ plane, as shown in Fig. 6 (b), and each valley locates between two

peaks. B_x and B_y are even and odd symmetrical around the $x=0$ plane, respectively. B_x and B_y for different D s have very similar distribution shapes, respectively. Their means have almost the same trend as their amplitudes, as shown in Fig. 6 (d). The amplitudes and means of B_x and B_y go up with the increase of D , demonstrating that smaller angle between the pipeline and the ambient field can cause more noticeable magnetic buckling characteristics.

C. Effects of temperature

Parametric sweeping is performed for the temperature 20 ~ 130°C. The background magnetic field

is with $I = 0^\circ$ and $D = 45^\circ$. The internal pressure is 10 MPa. The results are summarized and shown in Fig. 7. B_x and the norm B have similar distribution shapes, and both of them have two peaks at the two start points of the buckling section. When the temperature is lower than 50°C, B_y has two peaks symmetrically distributed about the $x=0$ plane; When the temperature is higher than 50°C, B_y has four peaks and two valleys symmetrically distributed about the $x=0$ plane, and each valley locates between two peaks. As the temperature exceeds 50°C and goes higher, characterizations of the pipe buckling by B_x and B_y become less and more noticeable, respectively.

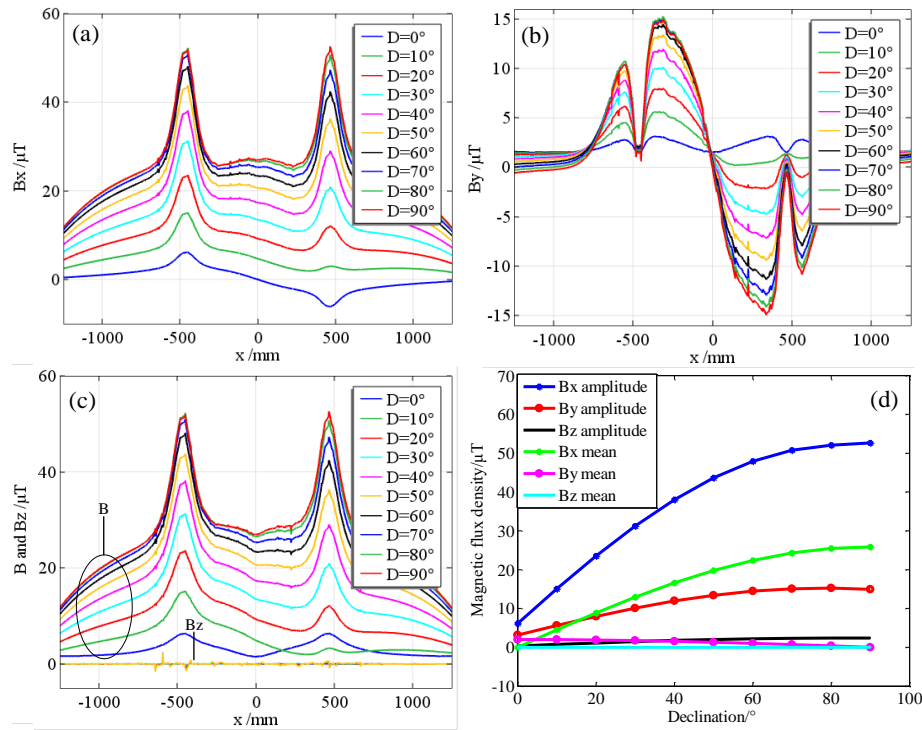


Fig. 6. Magnetic fields inside the buckling pipe under different directions of background magnetic fields: (a) B_x , (b) B_y , (c) B and B_z , and (d) amplitudes and means of the distributions of each component.

As shown in Fig. 7 (d), all the amplitudes and means of the magnetic components vary very slightly as the temperature increases except for B_x 's amplitude. This exception can be explained as follows. The internal pressure can cause hoop stress in the pipe wall and hence relieves the axial compressional stress resulting from the thermal expansion. At the two starts of the buckling section, the axial thermal stress is not easy to accumulate, so the axial and hoop expansions are comparable with each other. However, as the temperature is going higher and higher, the enhancing effects of the thermal expansion on the axial stress at first are smaller than and then exceed the weakening effects of the internal pressure. Therefore, the axial stress and the magnetic shielding at the buckling starts go down first and up then,

as the equivalent permeability goes down first and up then. The B_x component of the magnetic fields here therefore non-monotonically varies with the increase of D .

D. Effects of pressure

Parametric sweeping is performed for the internal pressure 0~20MPa with $I = 0^\circ$ and $D = 45^\circ$. The pipe temperature is 80°C. The results are summarized and shown in Fig. 8. B_x has two peaks at the two start points of the buckling section. B_y has four peaks and two valleys symmetrically distributed about the $x=0$ plane, and each valley locates between two peaks. B_x and B_y are even and odd symmetrical around the $x=0$ plane, respectively. The pressure only changes the overall magnetic intensity inside the buckling pipe, but does not change the magnetic

distribution modes along the axial line. That is because the stress in the pipe wall induced by the internal pressure is uniform and the permeability resulting from

the magnetomechanical effect is smoothly and evenly distributed.

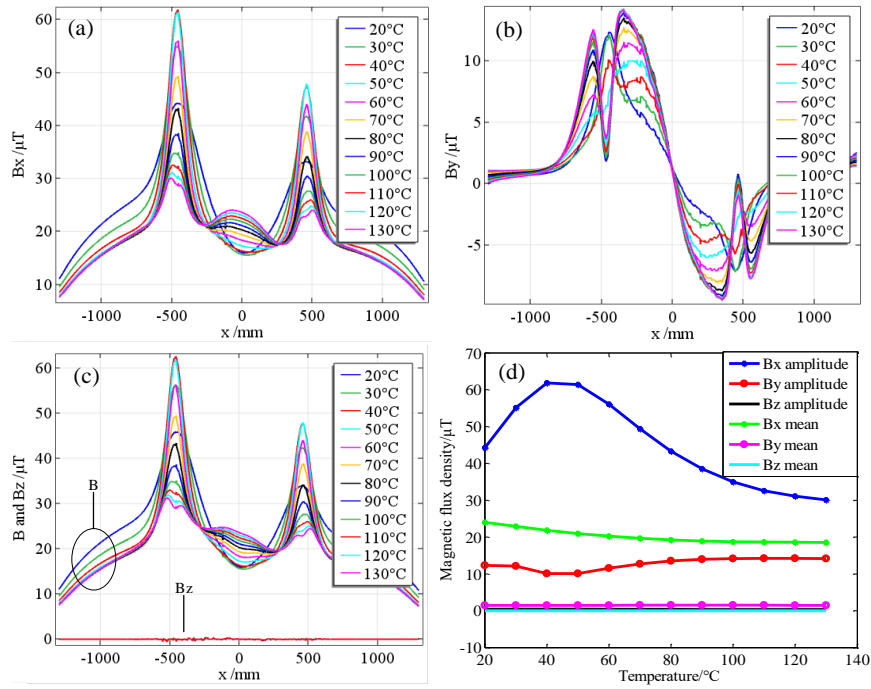


Fig. 7. Magnetic fields inside the buckling pipe with different temperatures: (a) B_x , (b) B_y , (c) B and B_z , and (d) amplitudes and means of the distributions of each component.

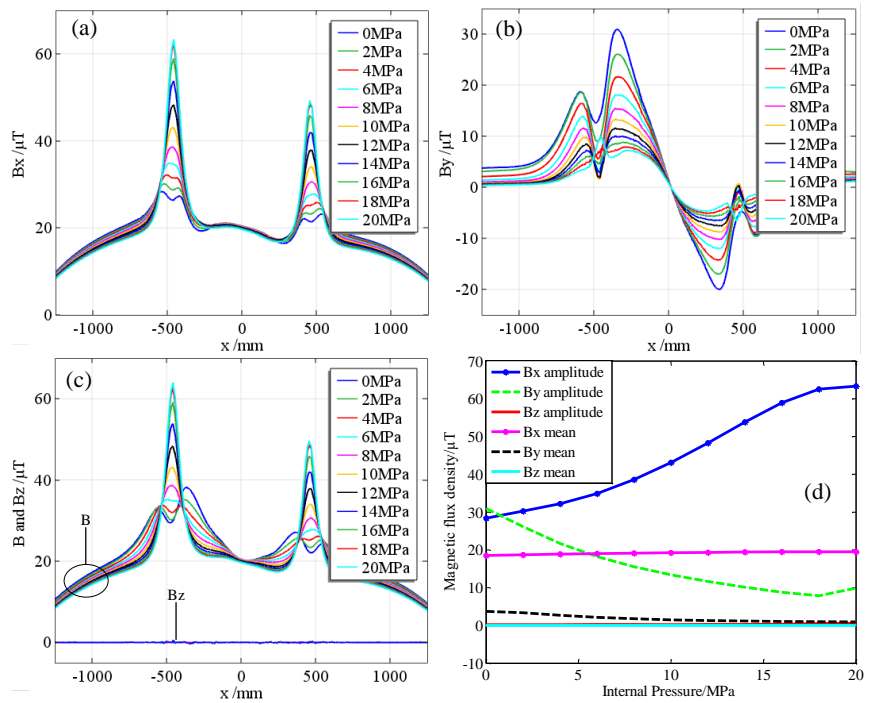


Fig. 8. Magnetic fields inside the buckling pipe with different internal pressures: (a) B_x , (b) B_y , (c) B and B_z , and (d) amplitudes and means of the distributions of each component.

Within this parameter configuration range, the weakening effect on the axial stress of the hoop expansion due to the internal pressure is always smaller than the enhancing effect of the thermal expansion. According to the stress calculation theory for thin-walled cylinder [19], the hoop strain monotonically increases with the increase of the internal pressure. Due to the Poisson effect, the axial stress is monotonically released. Therefore, the amplitude and mean of B_x and B_y components basically monotonously go up and down, respectively, with the increase of the internal pressure, as shown in Fig. 8 (d). In other words, if internal pressure is higher, the buckling characterization by B_x is better but worse by B_y .

E. Tiny buckling detection

In practice, a large pipeline buckling always starts from a tiny one that are very difficult to distinguish from their shape and appearance. It is preferable and very important to timely detect and predict the tiny buckling for early maintenance. Figure 9 shows the magnetic field distributions inside pipes under the same ambient field and pressure load, without and with considering the force magnetic effect, for the buckling deflections of 0 mm, 10 mm, 20 mm, and 30 mm.

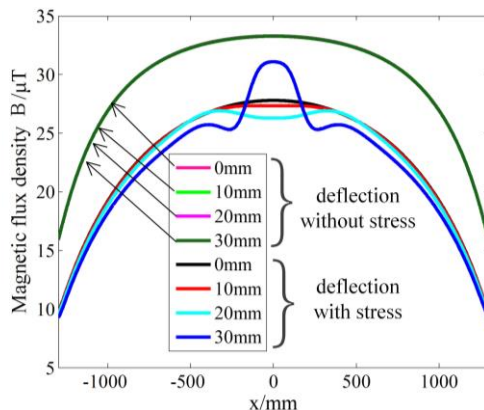


Fig. 9. Magnetic field distributions inside the tiny buckling pipes without and with stress considered.

When the magnetomechanical effect is not taken into account, all of the magnetic field distributions inside the pipes with deflections of 10mm, 20 mm, and 30 mm are the same to that of the straight pipe whose deflection is 0 mm. The tiny deformation without stress cannot be identified from the magnetic fields. When the permeability changes caused by the buckling stress are considered, the magnetic field distributions have noticeably local fluctuations in the middle of the buckling section, although the magnetic field values are a little smaller because the magnetic shielding becomes larger. Therefore, the results in Fig. 9 demonstrate that it is feasible to use the magnetic fields inside the pipelines to

detect the tiny buckling thanks to the magnetomechanical effect. This is very helpful for early diagnosis and prevention of pipeline bucklings.

V. CONCLUSIONS

(I) Magnetic fields inside the buckling pipe have many significant distribution characteristics that can be deployed to reliably and precisely identify the pipe buckling. B_x and B have similar even symmetric distribution shapes, and both have two peaks at the two start points of the buckling section. B_y has four peaks and two valleys odd symmetrically distributed about the middle vertical plane, and each valley locates between two peaks.

(II) These magnetic characteristics can be attributed to the complicated stress of the buckling section due to magnetomechanical effect. Internal pressure can cause hoop stress and hence relieve the axial compressional stress because of thermal expansion. The stress signs and magnitudes vary significantly in different cross-sections of the buckling pipeline, and reverse at the bend start. Higher internal pressures and temperatures seldom change the magnetic distribution shapes inside the buckling pipe, but indeed enhances the peak magnitudes. In addition, the results of each effect on magnetic behaviors/properties in the buckling pipe can be used as prior knowledges more reliably and precisely the pipe buckling by using these magnetic characteristics.

(III) It is feasible to use the magnetic fields inside the buckling sections to detect the tiny buckling with stress variances but without visible deformations thanks to the magnetomechanical effect. This is very helpful for early diagnosis and prevention of the pipeline bucklings.

ACKNOWLEDGMENT

This work was supported by National Natural Science Foundation of China (Nos. 51604192, 61773283, and 61473205).

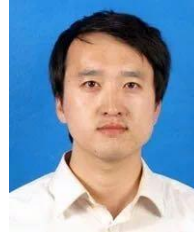
REFERENCES

- [1] Y. Liu, "Study on Transverse Thermal Buckling Mechanism and Control Measures of High Temperature/High Pressure Subsea Pipeline," *Ph.D. Thesis*, Dalian University of Technology, pp. 4-10, 2010.
- [2] N. F. Braathen and A. J. Sandford, *Pipeline Inspection by ROV*. Submersible Technology, Springer Netherlands, vol. 36, pp. 313-318, 1986.
- [3] W. Zeng, Y. Xu, L. Wan, and T. Zhang, "Optical vision pipeline inspection and tracking system for autonomous underwater vehicle," *Journal of Shanghai Jiao Tong University*, vol. 46, no. 2, pp. 178-183, 2012.
- [4] X. Huang, Y. Li, and S. Jin, "A control system based on data exchange using ethernet and CANBUS for deep water AUV," *IEEE: 9th Asian*

- Control Conference*, pp. 1-5, 2013.
- [5] J. Quarini and S. Shire, "A review of fluid-driven pipeline pigs and their applications," *Proceedings of the Institution of Mechanical Engineers, Part E: Journal of Process Mechanical Engineering*, vol. 221, no. 1, pp. 1-10, 2007.
- [6] H. S. Han, J. J. Yu, G. P. Chan, et al., "Development of inspection gauge system for gas pipeline," *Ksme International Journal*, vol. 18, no. 3, pp. 370-378, 2004.
- [7] M. S. Chowdhury and M. F. Abdelhafez, "Pipeline inspection gauge position estimation using inertial measurement unit, odometer, and a set of reference stations," *Sensors and Actuators B-Chemical*, vol. 2, no. 3, pp. 234-243, 2016.
- [8] M. Durali, A. Nabi, and A. Fazeli, "Design and simulation of an off-line internal navigation system for pipeline inspection applications," *ASME 2007 International Mechanical Engineering Congress and Exposition*, vol. 9, pp. 521-526, 2007.
- [9] W. Zhao, X. Huang, S. Chen, et al., "A detection system for pipeline direction based on shielded geomagnetic field," *International Journal of Pressure Vessels & Piping*, vol. 113, no. 1, pp. 10-14, 2014.
- [10] X. Huang, S. Chen, S. Guo, et al., "A 3D localization approach for subsea pipelines using a spherical detector," *IEEE Sensors Journal*, vol. 17, no. 6, pp. 1828-1836, 2017.
- [11] X. Huang, G. Chen, Y. Zhang, et al., "Inversion of magnetic fields inside pipelines: Modeling, validations, and applications," *Structural Health Monitoring-An International Journal*, vol. 17, no. 1, pp. 80-90, 2018.
- [12] J. Li, M. Xu, J. Leng, and M. Xu, "Metal magnetic memory effect caused by circle tensile-compressive stress," *Insight*, vol. 9, no. 25, pp. 142-145, 2011.
- [13] H. E. Stanley and V. K. Wong, "Introducing to phase transition and critical phenomena," *American Journal of Physics*, vol. 40, no. 6, pp. 927-928, 1972.
- [14] D. A. Kaminski, D. C. Jiles, S. B. Biner, M. J. Sablik, "Angular dependence of the magnetic properties of polycrystalline iron under the action of uniaxial stress," *Journal of Magnetism and Magnetic Materials*, vol. 291, pp. 382-384, 1992.
- [15] D. C. Jiles, "Theory of the magnetomechanical effect," *Journal of Physics D Applied Physics*, vol. 28, no. 8, pp. 1537-1546, 1995.
- [16] D. C. Jiles and L. Li, "A new approach to modeling the magnetomechanical effect," *Journal of Applied Physics*, vol. 95, no. 11, pp. 7058-7060, 2004.
- [17] G. Yicheng, *Ferromagnetic*. Peking University Press, pp. 8-11, 2014.
- [18] L. Peng, "Numerical analysis of buckling of high temperature and high pressure subsea pipelines

under coupling of pipe and soil," *Southwest Petroleum University*, pp. 57-59, 2014.

- [19] S. Zhifeng, "Gas pipeline special pipe section stress analysis and safety study," *China University of Petroleum (Hua Dong)*, pp. 18-19, 2009.



Zhang Yu received his B.E. and Ph.D. degrees in 2004 and 2009 from Tianjin University (TJU). He is now a Lecturer at TJU. His research interests cover detection technology and equipment.



Xue Yameng received her B.S. degree in 2016 in Taiyuan University of Technology. Now she is working toward her Master degree at TJU. Her research topics are pipeline localization.



Huang Xinjing received his B.S. and Ph.D. degrees in 2010 and 2016 at TJU. He is an Assistant Professor at TJU. His interests are magnetic analyses for pipeline damage detections. He is the corresponding author of this paper.



Li Jian received his B.E., M.E., and Ph.D. degrees in 1994, 1997 and 2000 from TJU. He is now a Professor at TJU. His research interests include pipeline leak detection and pipeline safety warning.



Chen Shili received his B.S. and Ph.D. degrees from TJU in 1997 and 2003. He is an Associate Professor at TJU. His research interests are novel online in-pipe detector.